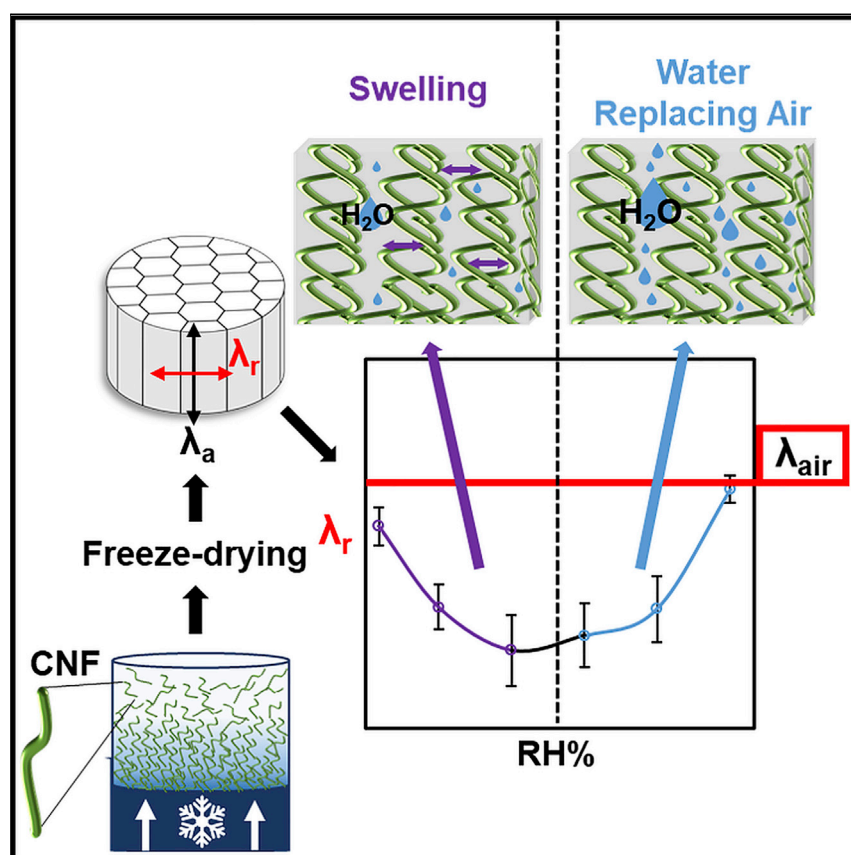


Article

Humidity-Dependent Thermal Boundary Conductance Controls Heat Transport of Super-Insulating Nanofibrillar Foams



We show that anisotropic foams based on aligned cellulose nanofibrils are super-insulating also at high relative humidity (RH). Thermal conductivity measurements and non-equilibrium molecular dynamic simulations show that the moisture-induced swelling and increase of the inter-fibrillar distance results in a reduction of the thermal boundary conductance that exceeds the thermal conductivity increase due to water uptake up to 75% RH. Phonon engineering by moisture could be used to tailor the heat transfer properties of hygroscopic nanofibrillar materials.

Varvara

Apostolopoulou-Kalkavoura,
Shiqian Hu, Nathalie Lavoine, ...,
Igor Zozoulenko, Junichiro
Shiomi, Lennart Bergström

lennart.bergstrom@mmk.su.se

HIGHLIGHTS

Anisotropic cellulose nanofibril
foams are super-insulating also at
high humidity

Moisture-induced swelling offsets
thermal conductivity increase due
to water uptake

Thermal boundary conductance
decreases 6-fold by increasing
inter-fibrillar gap

Thinner fibrils enhance phonon
scattering and reduce the thermal
conductivity

3

Understanding

Dependency and conditional studies
on material behavior

Apostolopoulou-Kalkavoura et al., Matter 4,
276–289

January 6, 2021 © 2020 The Authors. Published
by Elsevier Inc.

<https://doi.org/10.1016/j.matt.2020.11.007>



Article

Humidity-Dependent Thermal Boundary Conductance Controls Heat Transport of Super-Insulating Nanofibrillar Foams

Varvara Apostolopoulou-Kalkavoura,¹ Shiqian Hu,² Nathalie Lavoine,³ Mohit Garg,⁴ Mathieu Linares,^{4,5,6} Pierre Munier,¹ Igor Zozoulenko,^{4,7} Junichiro Shiomi,² and Lennart Bergström^{1,8,*}

SUMMARY

Cellulose nanomaterial (CNM)-based foams and aerogels with thermal conductivities substantially below the value for air attract significant interest as super-insulating materials in energy-efficient green buildings. However, the moisture dependence of the thermal conductivity of hygroscopic CNM-based materials is poorly understood, and the importance of phonon scattering in nanofibrillar foams remains unexplored. Here, we show that the thermal conductivity perpendicular to the aligned nanofibrils in super-insulating ice-templated nanocellulose foams is lower for thinner fibrils and depends strongly on relative humidity (RH), with the lowest thermal conductivity ($14 \text{ mW m}^{-1} \text{ K}^{-1}$) attained at 35% RH. Molecular simulations show that the thermal boundary conductance is reduced by the moisture-uptake-controlled increase of the fibril-fibril separation distance and increased by the replacement of air with water in the foam walls. Controlling the heat transport of hygroscopic super-insulating nanofibrillar foams by moisture uptake and release is of potential interest in packaging and building applications.

INTRODUCTION

Insulation materials frequently used in buildings and in packaging, such as gas-filled polyurethane foams or expanded polystyrene (EPS), are derived from fossil sources and use hazardous precursors.¹ Biobased insulation materials with thermal conductivities below those of polyurethane or EPS ($20\text{--}40 \text{ mW m}^{-1} \text{ K}^{-1}$) could both reduce the carbon footprint of thermal insulation materials and the energy needed for heating or cooling. Cellulose nanomaterials (CNMs) are renewable materials characterized by a low density, high strength and stiffness,² tunable surface chemistry, and relatively low thermal conductivity,^{3,4} and are thus excellent candidates for non-fossil-derived insulation materials. CNMs in the form of cellulose nanofibrils (CNFs) consist of cellulose molecules packed together into long, partially crystalline fibrils with diameters ranging between 3 and 40 nm and aspect ratios larger than 100.^{5,6} Cellulose occurs abundantly in wood, primarily as crystalline cellulose I β , which has a two-chain monoclinic unit cell.^{7,8} The thermal conductivity of cellulose I β is several times higher along the covalently bonded chain direction (c-axis), compared with the transverse direction where weaker interactions connect the adjacent chains.^{9,10} The alignment of cellulose in wood¹¹ results in materials with anisotropic heat transport properties, similar to other aligned 1D and 2D nanomaterials such as bulk carbon allotropes,¹² carbon nanotubes,¹³ single-layer black phosphorene,¹⁴ drawn oriented polyethylene,¹⁵ and graphene.^{12,16,17} Anisotropic heat transport properties are of interest in applications where directional heat management is

Progress and Potential

Efficient thermal insulation using biobased materials could reduce the energy consumption and minimize the carbon footprint of buildings. Biobased materials are sensitive to moisture, and there is a need to better understand how moisture controls the thermal conductivity. Here, we show that anisotropic cellulose nanofibril foams can be super-insulating also at high humidity. The relative humidity dependence of the thermal conductivity of super-insulating nanocellulose foams is controlled by moisture-induced phonon scattering and the replacement of air with water. The moisture-induced swelling and increase of the inter-fibrillar separation distance results in a reduction of the thermal boundary conductance that exceeds the thermal conductivity increase due to water uptake up to high relative humidity. Humidity-dependent phonon engineering could be used to tailor the heat transfer properties of biobased nanofibrillar materials for packaging and thermal management in buildings.

required; e.g., cooling of electronic circuits and potentially also in packaging and buildings.

Traditionally, cellulose has been used as an insulation material¹ in the form of sawdust, cotton, and recycled newspaper, but the thermal conductivities of 40–60 mW m⁻¹ K⁻¹ are insufficient for many applications. Lightweight nanocellulose-based materials such as isotropic CNM aerogels,^{18–20} spray-freeze-dried aerogels,²¹ Pickering CNF aerogels,²² silylated CNF-silica scaffolds,²³ and CNF-nanozeolites composite aerogels²⁴ can display thermal conductivities significantly lower than those of traditional EPS insulation and even below that of air (=25.7 mW m⁻¹ K⁻¹) at ambient conditions. Cellulose and CNM-based materials are hygroscopic,^{11,25} and the thermal conductivity of isotropic foams at room temperature (RT) increases with increasing relative humidity (RH) as adsorbed water replaces air.^{1,26} The elasticity and strength of CNF films are also strongly reduced at high RH.²⁷ Molecular dynamics simulations suggest that inter-fibrillar hydrogen bonds may weaken or break with increasing RH due to competition with the adsorbed water molecules.^{27–29}

Recently, it was demonstrated that low-density CNF-based foams with aligned nanofibrils and columnar macropores display strongly anisotropic^{30,31} and RH-dependent³² heat transport properties, with a minimum radial thermal conductivity of the CNF foams, perpendicular to the fibril and macropore direction, of 18 mW m⁻¹ K⁻¹. Such low thermal conductivities have only been attained in nanoporous materials, such as silica aerogels,^{33,34} where pore sizes below the mean free path length of air can result in thermal conductivities substantially below the value for air. Phonon scattering at the interfaces between nanosized materials can also reduce the thermal conductivity, and it was recently shown that tuning the separation distance in, for example, few-layer graphene¹⁷ or multi-layer graphene,³⁵ and the water density at weakly bonded interfaces of self-assembled monolayers^{36,37} can have a strong influence on the thermal boundary conductance of nanomaterials. Hence, it would be important to determine the contribution and importance of phonon scattering to the moisture-dependent thermal conductivity of anisotropic foams. However, the understanding of how RH and moisture uptake controls the thermal conductivity of hygroscopic anisotropic nanofibrillar-based foams is poor and the thermal boundary conductance of CNM-based materials has not been investigated previously.

Here, we have combined thermal conductivity measurements and molecular simulations to quantify the effect of RH on the anisotropic heat transfer and thermal boundary conductance of ice-templated CNF foams with highly aligned nanofibrils of different diameters in the foam walls. The RH dependence of the thermal conductivity of hygroscopic nanocellulose foams was shown to be controlled by moisture-induced phonon scattering and the replacement of air with water. The moisture-induced swelling and increase of the inter-fibrillar separation distance can result in a 6-fold reduction of the thermal boundary conductance that exceeds the thermal conductivity increase due to water uptake up to high RH. Foams made from thinner fibrils display lower thermal conductivities due to enhanced phonon scattering. Understanding how heat transport of biobased nanofibrillar foams can be tuned by moisture uptake and release could enable novel ways to engineer hygroscopic super-insulating nanomaterials in packaging and building applications.

RESULTS

CNFs and Ice-Templated Foams

Low-density foams were produced by ice templating aqueous suspensions of CNFs. We used three different CNFs that differed primarily in the degree of carboxylation

¹Department of Materials and Environmental Chemistry, Stockholm University, 106 91 Stockholm, Sweden

²Department of Mechanical Engineering, The University of Tokyo, 7-3-1 Hongo, Bunkyo-ku, Tokyo 113-8656, Japan

³Department of Forest Biomaterials, College of Natural Resources, NC State University, Campus Box 8005, Raleigh, NC 27695, USA

⁴Laboratory of Organic Electronics, ITN, Linköping University, 581 83 Linköping, Sweden

⁵Scientific Visualization Group, ITN, Linköping University, 581 83 Linköping, Sweden

⁶Swedish e-Science Research Centre (SeRC), Linköping University, 581 83 Linköping, Sweden

⁷Wallenberg Wood Science Center, Linköping University, 581 83 Linköping, Sweden

⁸Lead Contact

*Correspondence:
lennart.bergstrom@mmk.su.se
<https://doi.org/10.1016/j.matt.2020.11.007>

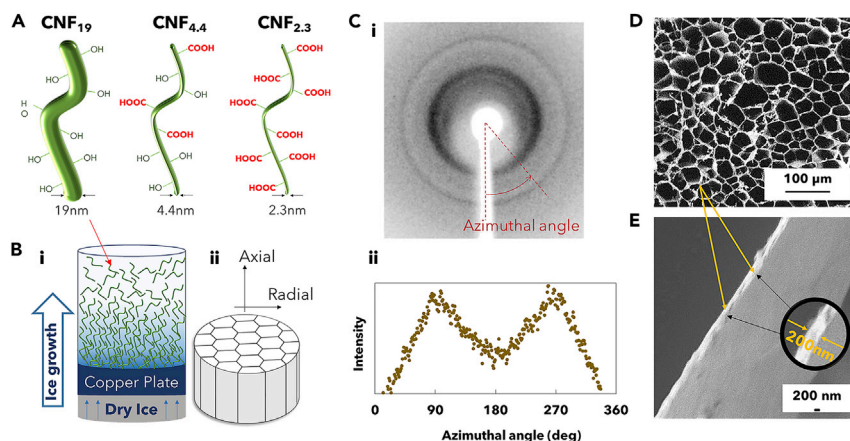


Figure 1. Preparation and Structure of Ice-Templated Anisotropic CNF Foams

(A) Schematic illustration of the CNF morphology, diameter, and surface chemistry.
(B) Schematic illustration of: (i) the ice-templating process; (ii) the anisotropic foam structure.
(C) XRD investigation of CNF_{2.3} foams showing: (i) 2D diffraction pattern; (ii) azimuthal intensity profiles.
(D) SEM image of the radial cross section of the ice-templated CNF_{2.3} foams.
(E) HRSEM image of a CNF_{2.3} foam wall.

at the C6 positions in the anhydroglucose units and the diameter (d) and length (L) of the fibrils (Figure 1A). X-ray diffraction (XRD) and atomic force microscopy (AFM) image analysis (Figure S1), together with conductometric titration and sedimentation measurements³⁸ of non-oxidized CNFs with an average diameter of 19 nm (CNF₁₉), medium-charge 2,2,6,6-tetramethylpiperidine-1-oxyl radical (TEMPO)-oxidized CNFs with an average diameter of 4.4 nm (CNF_{4.4}), and high-charge TEMPO-oxidized CNFs with an average diameter of 2.3 nm (CNF_{2.3}) showed that more intensive oxidation led to smaller fibril diameter, higher aspect ratio (L/d ; Equation S1 and S2), and lower crystallinity index (Equation S3) (Table 1).

Directional growth of the ice crystals during freeze-casting resulted in strongly anisotropic foams with the CNF particles aligned in the growth direction of the ice crystals (Figure 1B). The nanofibril alignment was confirmed by 2D XRD patterns and azimuthal integration (Figure 1C, Equations S4 and S5), and is consistent with previous studies on CNM-based freeze-cast foams.^{39,40} The SEM images of the cross section along the radial direction (Figure 1D) of the CNF foams showed a porous honeycomb-like architecture with a narrower pore size distribution in the CNF_{2.3} foams (Figure 1E) than in the CNF₁₉ (Figure S2A) or CNF_{4.4} (Figure S2B) foams. The macroporous structure of freeze-cast materials is determined predominantly by the confined growth of the ice crystals, and the nanoporous structure within the pore walls is strongly influenced by the ability of the particles to be transported and assembled as the freezing front moves through the dispersion.⁴⁰

The nanoporosity, I_{np} , of the foams corresponds to pores with sizes between 2 and 100 nm. CNFs with low charge density (CD) display electrostatic repulsions that may be of insufficient magnitude to prohibit the CNF particles from aggregating during ice templating and therefore result in foams with disordered structures.⁴¹ CNFs with high CD (i.e., 1.6 mmol COO[−]g^{−1}) display strong interparticle repulsion⁴¹ and produce ordered ice-templated structures (Figure 1D). High-resolution scanning electron microscopy (HRSEM) showed that the foam walls of the highly charged CNF_{2.3} foam were compact and thin, with a thickness of about 200 nm (Figure 1E).

Table 1. Physical Properties of CNF₁₉, CNF_{4.4}, and CNF_{2.3} at 295 K

	CD ^a (mmol COO ⁻ g ⁻¹)	Crystallinity index ^b (%)	Diameter ^c d (nm)	Aspect ratio ^d L/d
CNF ₁₉	0.02 ± 0.004	54	19 ± 7.9	110 ± 26
CNF _{4.4}	0.30 ± 0.020	52	4.4 ± 1.8	140 ± 4
CNF _{2.3}	1.60 ± 0.010	45	2.3 ± 0.7	200 ± 16

^aCD was measured by conductometric titration.^bCrystallinity was measured by XRD.^cd was measured by AFM image analysis.^dAspect ratio was measured by sedimentation.

The difference in the Brunauer-Emmett-Teller (BET) surface area between the CNF_{2.3} foam (15 m²/g) and the CNF₁₉ foam (8.7 m²/g; Figure S3) is much smaller than the >60-fold difference predicted based upon the fibril diameters, which suggests that the fibrils in the walls are tightly packed. Nitrogen sorption experiments (Figure S3) performed at dry conditions show that the foam walls contain a low fraction (3.5%–5%) (Equation S6 and S7, Table S1) of pores up to 12 nm (Figure S3C) in diameter.

Thermal Conductivity

The radial (λ_r) and axial (λ_a) thermal conductivities of the CNF₁₉, CNF_{4.4}, and CNF_{2.3} ice-templated foams (Figure 2A) with a dry density between 5.9 and 6.4 kg m⁻³ were measured using the anisotropic mode of the Hot Disk at controlled temperature and RH (Figures S4A and S4B). The hot disk records the time-dependent temperature increase in response to a transient power pulse and determines the radial thermal diffusivity (α_r , Figure S4C). The radial thermal conductivity, λ_r is calculated by Equation 1⁴²:

$$\lambda_r = \alpha_r \rho C_p \quad (\text{Equation 1})$$

where C_p is the specific heat capacity of the foam, and ρ is the density of the foam. The “dry” C_p ($RH = 0$) is determined from differential scanning calorimetry (DSC) measurements (Figure S5), and the RH -dependent C_p at $RH > 0$ is estimated by the rule of mixtures (Equation S12) taking into account the water uptake (Figure 3A) of the foam and the C_p of water. The C_p at dry ($RH = 0$) conditions decreased with increasing CD (and decreasing diameter) of the CNFs, from 1,180 to 753 J kg⁻¹ K⁻¹ for CNF₁₉ and CNF_{2.3}, respectively (Figure S5). The axial thermal conductivity is measured in the direction of the ice crystal growth and thus the direction of the columnar macropores, while the radial thermal conductivity is measured perpendicularly to the macropores and the aligned CNFs.

The thermal conductivities of the ice-templated CNF foams were anisotropic and depended strongly on the RH. The λ_r (Figure 2B) of the CNF foams were 3–10 times lower than λ_a (Figures S4D and S4E) depending on the RH and the diameter of the CNFs. The anisotropy of the thermal conductivity of the ice-templated foams is related to the alignment of the nanofibrils in the freezing direction (Figures 1C and S6) and the intrinsic anisotropy of the thermal conductivity of cellulose. The λ_r of the ice-templated foams decreased with an increase of RH up to 35%–50% RH and increased as the RH increased from 65% to 80% RH (Figure 2B). Freeze-cast foams prepared from CNFs with the smallest diameter (CNF_{2.3}) displayed a lower λ_r compared with foams prepared from CNFs with larger diameter and lower CD (Figure 2B), and the lowest thermal conductivity (14 mW m⁻¹ K⁻¹) was attained at 35% RH for the CNF_{2.3} foam. This value of the radial thermal conductivity is significantly below the value for air ($\lambda = 25.7$ mW m⁻¹ K⁻¹), which is surprising considering that the majority of the pores of ice-templated foams are much larger than the mean

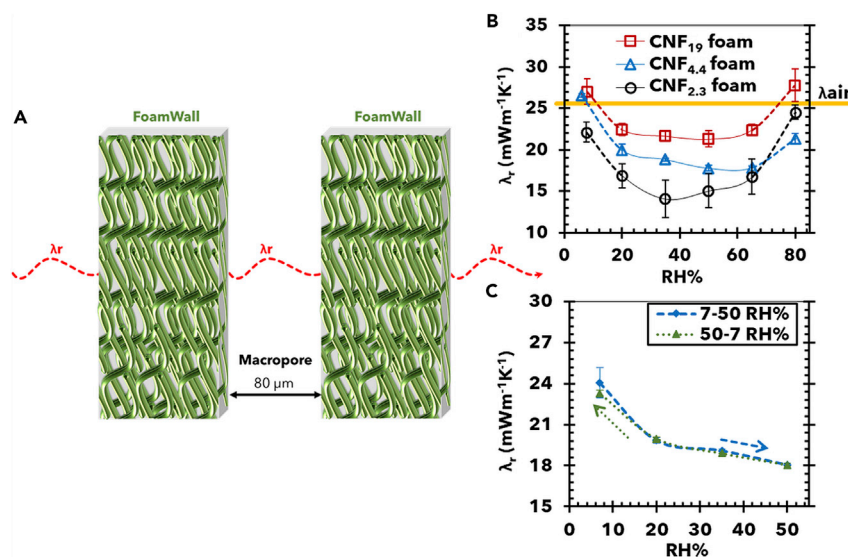


Figure 2. Thermal Conductivity of Anisotropic CNF Foams

(A) Schematic illustration of the structure of two foam walls and representation of the radial thermal conductivity (λ_r).

(B) Radial thermal conductivity (λ_r) of ice-templated CNF_{2.3}, CNF_{4.4}, and CNF₁₉ foams as a function of RH at 295 K.

(C) Reversible radial thermal conductivity (λ_r) of ice-templated CNF_{4.4} foams as a function of RH at 295 K, for 7% to 50% RH (dashed line) and for 50% to 7% RH (dotted line).

free path of air (about 70 nm in open space).^{19,43,44} The convection contribution should be negligible because the macropores are sufficiently small to minimize gas transport over large distances and the radiation contribution is also small at RT (295 K).^{44,45} The presence of nanopores in the foam walls is expected to reduce the gas conduction contribution, but it is clear that additional effects, such as a substantial decrease of the thermal boundary conductance by phonon scattering, need to be invoked to explain the very low thermal conductivities.

The λ_r of the anisotropic freeze-cast CNF foams remained below the thermal conductivity of air between 10% and 70% RH (Figure 2B) and was always several times lower than λ_a (Figures S4D and S4E). In contrast, λ_a increased with increasing RH over the entire measured range (7%–80% RH) for all of the CNF foams (Figures S4D and S4E), similar to isotropic CNF- and polyoxamer-based foams.²⁶ Figure 2C shows that the effect of RH on λ_r was reversible between 7% and 50% RH, which suggests that the moisture uptake is reversible²⁹ and that the structure of the foam walls is not irreversibly affected by the moisture uptake within the investigated RH range. Thermal conductivity measurements (Table S2) on CNF_{4.4} foams with a high density (9.2 kg m^{−3} at 0% RH) showed that the radial thermal conductivity is slightly higher but remains below the super-insulating level and maintains a similar parabolic RH behavior as for the CNF_{4.4} foams shown in Figure 2B (with a density of 6.4 kg m^{−3} at 0% RH).

Moisture Uptake and Swelling

The moisture uptake of the ice-templated CNF foams increased with increasing RH (Figures 3A and S7A). The foams with the thinnest fibrils (i.e., the CNF_{2.3} foam) took up more moisture than the foams with thicker fibrils (i.e., the CNF₁₉ and CNF_{4.4} foams), which suggests that water uptake is primarily controlled by adsorption onto the CNF surfaces.

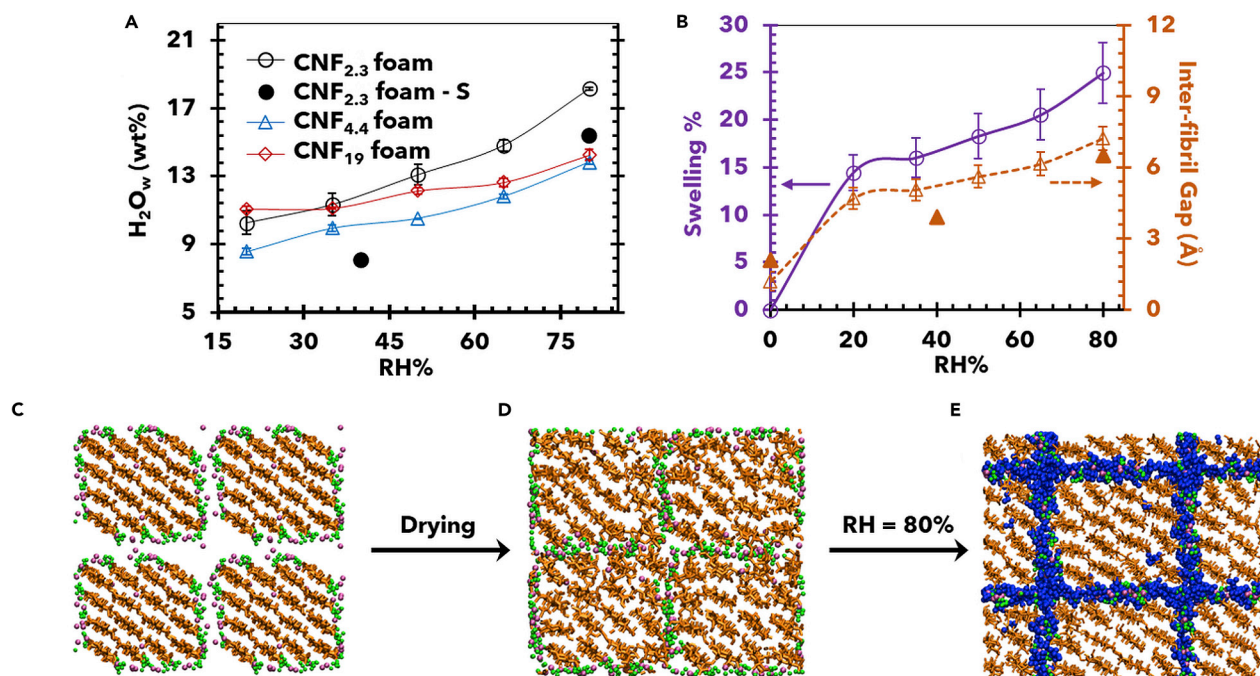


Figure 3. Experimental and Hybrid GCMC/MD Simulations of Moisture Uptake and Foam-Wall-Sorption-Induced Swelling

(A) Experimental moisture content (H_2O_w) by mass of ice-templated foams prepared from CNF_{2.3}, CNF_{4.4}, and CNF₁₉ compared with the moisture content obtained from hybrid GCMC/MD simulations for the CNF_{2.3} (CNF_{2.3}-S) as a function of RH% at 295 K.

(B) The estimated swelling (continuous line-O) and average inter-fibril gap (dashed line-Δ) of a CNF_{2.3} foam as a function of RH%.

(C–E) (C) Initial arrangement of four individually equilibrated fibrils before drying. Snapshots of cellulose bundle of (D) aligned CNF_{2.3} fibril after the drying when they come close to each other, and (E) the same fibrils subjected to RH that have swelled as water molecules have entered their interstitial sites. Cellulose chains are colored in orange, COO[−] groups in green, counterions in pink, and water in blue.

With increasing RH, the water uptake induced swelling and an increase in the nanoporosity of the CNF foam walls (Table S1). The nanoporosity of the dry foam walls (RH = 0), estimated from nitrogen sorption data (Figure S3B), did not differ much between the different ice-templated foams (Table S1) at RH = 0. However, the estimated nanoporosity of the CNF_{2.3} foam increased significantly with increasing RH and it was higher compared with the nanoporosities of the wet CNF_{4.4} and CNF₁₉ foams (Table S1).

The fibril-fibril separation distance was estimated from the diameter of the fibrils and the porosity of the foam walls, which depends on the RH and the associated water uptake and swelling. We estimated the fibril-fibril separation distance, g_i , using a simple geometric approach (Equation 2),

$$g_i = \frac{\Pi_{np}}{(1 - \Pi_{np})} d_{CNF} \quad (\text{Equation 2})$$

where Π_{np} is the RH-dependent nanoporosity (Equation S6, Table S1) and d_{CNF} is the CNF diameter (Table 1). The fibril-fibril separation distance increased significantly when RH increased from 0 to 20%; from 1.2 to 4.7 Å for CNF_{2.3}, from 1.9 to 7.4 Å for CNF_{4.4} and from 6.8 to 37 Å for CNF₁₉ (Figures 3B, S7B, and S7C). Between 20% and 80% RH, the increase in fibril-fibril separation distance was lower, reaching estimated values of 7.4 Å for CNF_{2.3}, 10.8 Å for CNF_{4.4} and 46 Å for CNF₁₉ at 80% RH (Figures 3B, S7B, and S7C).

The increase of the foam wall thickness, the one-dimensional swelling (Sw), can be estimated using Equation 3, assuming that Sw (in percent) is directly related to the change in fibril-fibril separation distance:

$$\%Sw = (1 - \Pi_{np0}) \times \left(\frac{g}{d_{CNF}} + 1 \right) - 1 \quad (\text{Equation 3})$$

where, Π_{np0} is the nanoporosity at $RH = 0\%$ (Equation S6 and S7). The foam wall swelling at 80% RH was around 20% for the $CNF_{4.4}$ and CNF_{19} foams and about 26% for the $CNF_{2.3}$ foams, which corresponds to an estimated increase of the thickness of the foam wall from 200 to 250 nm.

Moisture-induced swelling of the fibril bundles was investigated using Grand Canonical Monte Carlo Simulation (GCMC) and Molecular Dynamics (MD) simulations. A bundle of aligned cellulose fibrils, each of which contained cellulose chains arranged in a β crystal lattice with an approximate square cross section, were considered and the RH was varied through changes of the chemical potential (μ , Equations S13 and S14) of the system.

Figure 3C shows four individually equilibrated fibrils with carboxylate surface groups and Na^+ counterions. Upon drying, the fibers come closer to each other, as illustrated in Figure 3D. Increasing the chemical potential/ RH resulted in moisture uptake, swelling, and an increase of the fibril-fibril separation distance (Figures 3B and S8); Figure 3E shows a snapshot corresponding to an RH of 80%. The water uptake at 40% and 80% RH that was obtained from the hybrid simulations (Figure 3A) corresponded relatively well with the measured water uptake of the CNF foams (Figure 3A), and a CNF film and CNF foam of higher density (Figure S7A). The fibril-fibril separation distances estimated from the experimental data (Equations 2 and 3) are in good agreement with the separation distances at 40% (4.0 Å) and 80% (6.5 Å) RH (Figure 3B) obtained by GCMC/MD simulations, which suggests that the microstructural changes in the hygroscopic foam walls can be attributed to moisture-induced swelling and that the simple geometric approach provides a reasonable estimate of the fibril-fibril separation distance.

The simulations of square fibrils were complemented with a similar study on hexagonal cellulose fibrils arranged in a hexagonal bundle, as shown in Figure S9A. The inter-fibril separation distance in the hexagonal bundle immersed in water reached an equilibrium distance of ≈ 7.5 Å (Figures S9B–S9D), which corresponded well with the GCMC/MD simulation results on the square bundles. Hence, water uptake and swelling did not depend on the shape or arrangement of the fibrils. Furthermore, the total energy of the system as a function of time is shown in Figure S10. The total energy of the system decreases during the course of the simulation until it reaches a saturation value, which ensures that the system has reached an equilibrium.

Thermal Boundary Conductance

The thermal boundary conductance at the interface between two cellulose slabs with the cellulose chains organized parallel to one another separated by a gap that can contain varying amounts of water has been estimated as a function of the gap distance by non-equilibrium molecular dynamics (NEMD) simulations (Figure 4). The thermal boundary conductance, TBC , is calculated from Equation 4,

$$TBC = -\frac{J}{\Delta T}, \quad (\text{Equation 4})$$

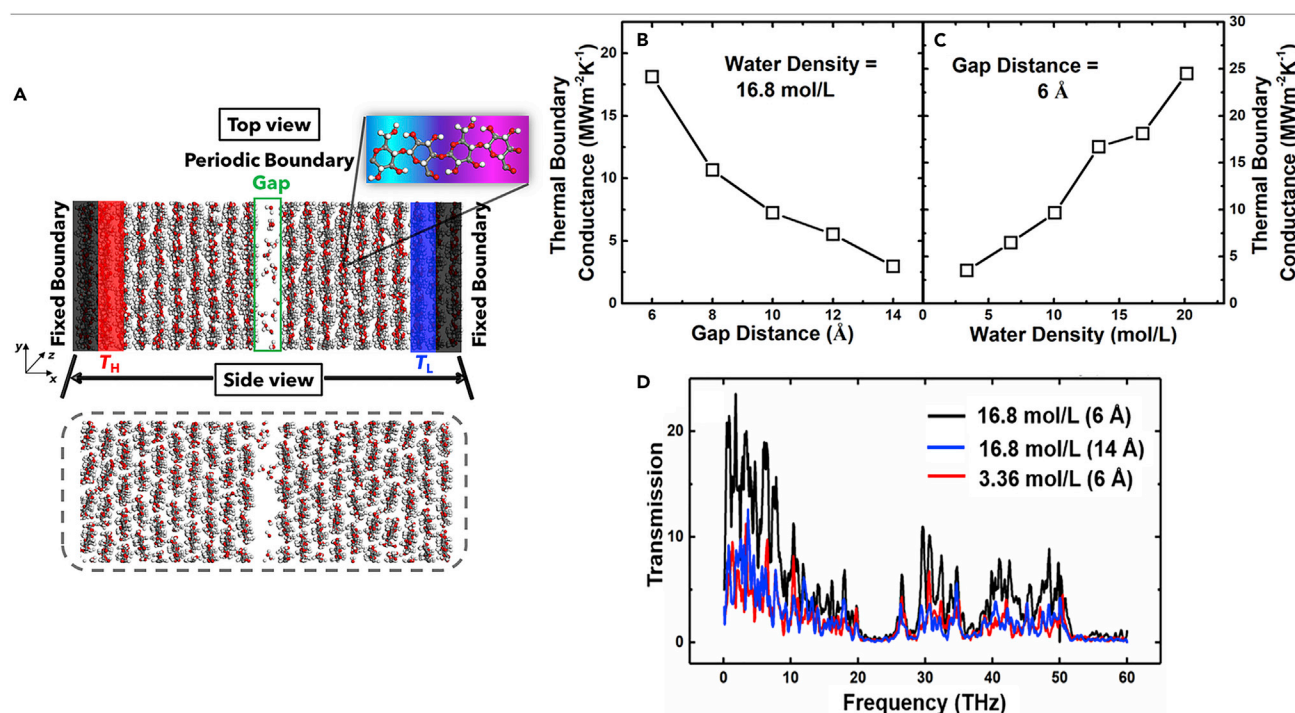


Figure 4. Thermal Boundary Conductance of CNFs

(A–C) (A) Schematic of the system examined by NEMD simulation, showing top and side views of two cellulose slabs separated by a gap with a variable distance. Fixed boundary conditions are applied along the x direction, while periodic boundary conditions are applied along the y and z directions. Thermal boundary conductance at RT estimated by NEMD simulations (B) as a function of gap distance at 16.8 mol/L water density, and (C) as a function of water density at 6 Å gap distance.

(D) Frequency dependence of the phonon transmission with 16.8 mol/L water density and 6 Å gap distance (black line), 16.8 mol/L water density, and 14 Å gap distance (blue line) and 3.36 mol/L water density and 6 Å gap distance (red line).

where ΔT and J are the temperature difference and the heat flux across the interface, respectively.

The simulated system (Figure 4A) mimics the interface between the aligned CNFs in the foam walls and offers the possibility to probe how the variation of the distance between the nanofibrils and the water content in the gap will affect the thermal boundary conductance. Indeed, Figure 3 shows that minor changes in RH can result in significant changes of the fibril-fibril separation distance. We have modeled the cellulose fibrils on each side of the interface as single crystals, because having termini with uniform thermal conductivity in NEMD simulations makes the extraction of thermal boundary conductance straightforward. The inter-fibril separation distance was modeled as a gap between the slabs (green rectangle in Figure 4A), and was varied from 6 to 14 Å. The lower value for the gap, 6 Å, is similar to the estimated fibril-fibril separation distance in CNF₁₉ at RH = 0% (6.8 Å) and within the range observed for CNF_{2,3} (Figures 3B and S7C). The NEMD simulations show that the thermal boundary conductance between the two cellulose slabs decreased by a factor of six as the gap distance increased from 6 to 14 Å at a fixed water density of 16.8 mol/L (Figure 4B). The effect of water was modeled by randomly inserting water molecules in the gap at a given molar density.

For a fixed gap distance of 6 Å, the thermal boundary conductance increased with a factor of six as the water density increased from 3.4 to 20.1 mol/L (Figure 4C). Hence, the

NEMD simulations show that the thermal boundary conductance between cellulose surfaces is strongly influenced by the gap distance and water density, suggesting the RH dependence of the thermal conductivity of the CNF foams (Figure 2B) is determined by the competing effects of swelling, which reduces the thermal boundary conductance (Figure 4B), and the replacement of air with water, which increases the thermal boundary conductance (Figure 4C). Indeed, for $RH < 20\%$, the increase of the gap distance with increasing RH dominates over the relatively small increase of the water content in the gap (Figure 3B) and thus results in a decrease of thermal boundary conductance (Figure 4B), which can explain the decrease of the thermal conductivity of the CNF foams in this RH range (Figure 2B). For $RH \gtrsim 40\%$, the observed increase of the thermal conductivity with increasing RH (Figure 2B) corresponds to the significant increase of the thermal boundary conductance (Figure 4C) caused by the increase in the water content in the inter-fibrillar gap, and the relatively small increase of the gap distance.

To gain further insight into the transmission and scattering of phonons in nanofibrillar assemblies, we calculated the spectral phonon transmission (Equation S15 and S16)⁴⁶ at the interface of two nanocellulose fibrils. Figure 4D shows that the low-frequency phonons (<10 THz) are more easily transmitted through the interface than the high-frequency phonons. Phonon transmission is also significantly suppressed for nearly the entire frequency range as the gap distance increases at constant water density. In contrast, when the gap distance is fixed at 6 Å, the phonon-transmission function increases with the water density.

DISCUSSION

Thermal conductivity measurements and molecular simulations have shown that the anisotropic heat transfer and thermal boundary conductance of super-insulating ice-templated CNF foams is controlled by moisture-dependent phonon scattering and the replacement of air with water. The moisture-induced swelling and increase of the inter-fibrillar separation distance results in a significant reduction of the thermal boundary conductance that exceeds the thermal conductivity increase due to water uptake. The anisotropic nanofibrillar foams are super-insulating also at high RH and the minimum radial thermal conductivity of $14 \text{ mW m}^{-1} \text{ K}^{-1}$ at 35% RH is the lowest reported for ice-templated CNF foams, much lower than commercially available insulating materials such as EPS and polyurethane, and similar to silica aerogels. Foams of high-charge-density CNFs with a small diameter display a lower thermal conductivity than foams of low-charge CNFs with a large diameter, which suggests that a larger number of interfaces in the foam walls of aligned thin fibrils enhances the phonon scattering contribution.

The humidity-dependent phonon scattering properties of anisotropic CNF foams suggest that tailoring the hygroscopic properties and the related dimensional changes of nanofibrillar assemblies could be of potential interest in packaging applications and for thermal management in buildings. The possibility to phonon-engineer nanomaterials by moisture uptake and release could be extended to other hygroscopic nanofibrillar materials (e.g., biopolymer-based materials such as chitin and silk), and 1D and 2D inorganic nanomaterials (e.g., clays and metal oxide whiskers).

EXPERIMENTAL PROCEDURES

Resource Availability

Lead Contact

Further information and requests for resources and reagents should be directed to, and will be fulfilled by, the Lead Contact, Lennart Bergström (lennart.bergstrom@mmk.su.se)

Materials Availability

This study did not generate new unique reagents.

Data and Code Availability

The published article includes all datasets generated or analyzed during this study.

Materials

A never-dried sulfite softwood cellulose pulp (Domsjö dissolving Plus) was provided by Domsjö Fabriker AB (Aditya Birla Domsjö, Sweden) and used as starting material. NaClO (Alfa Aesar), 2,2,6,6-tetramethyl-1-piperidinyloxy free radical (TEMPO, $\geq 98\%$, Alfa Aesar), sodium hydroxide (NaOH, P99.2%, VWR Chemicals), sodium bromide (NaBr, BioUltra, P99.5%, Sigma-Aldrich) and sodium borohydride (NaBH_4 , $\geq 98\%$, Sigma-Aldrich) were used as received.

Preparation of CNF Suspensions

The $\text{CNF}_{2.3}/\text{CNF}_{4.4}$ were prepared as previously reported using the TEMPO/NaBr/NaClO system with 2.5 and 10 mmol of NaClO per gram of cellulose.⁴⁷ The TEMPO-mediated oxidation was performed at pH 10 (reaction time up to 4 h). Residual aldehyde and ketone groups in the TEMPO-oxidized cellulose (TC) pulps were reduced by adding 0.1 g of NaBH_4 per gram of cellulose to the TC suspension at pH 10 and allowing it to stir for 3 h.⁴⁸ The TC pulps obtained were washed thoroughly with deionized water (DI) to remove excess reagents.

The $\text{CNF}_{2.3}/\text{CNF}_{4.4}/\text{CNF}_{19}$ were obtained by grinding the TC using a supermasscolloider grinder (Model MKZA10-15J, Masuko Sangyo Co., Ltd, Japan) equipped with non-porous grinding stones containing silicon carbide (Disk model MKE), using a gap clearance of $-100\text{ }\mu\text{m}$ at a motor frequency of 30 Hz.

The CD was determined by conductometric titration to be 0.02, 0.30, and 1.60 mmol COO^- per gram of cellulose for CNF_{19} , $\text{CNF}_{2.3}$, and $\text{CNF}_{4.4}$ respectively.⁴⁹

Preparation of Anisotropic CNF Foams

Anisotropic CNF foams were prepared by unidirectional ice templating^{30,39} from dispersions of $\text{CNF}_{19}/\text{CNF}_{2.3}/\text{CNF}_{4.4}$ diluted to 0.5 wt % in deionized water. Teflon molds 4 cm in diameter and 2.5 cm in height and with copper bottom plates were filled with CNF dispersion and placed in contact with dry ice, giving a cooling rate of 3 K min^{-1} . The final dry foams were obtained by ice sublimation at 0.024 mbar and RT for 4 days using a freeze dryer (Christ Alpha 1-2LDplus, Germany).

CNF Characterization

AFM (Dimension 3100, Bruker, United States) operated in tapping mode was used to determine the CNF dimensions (Figure S1). A droplet of 0.001–0.005 wt % aqueous CNF dispersion was deposited onto freshly cleaved mica substrate and dried at RT.

Sedimentation experiments were conducted to determine the aspect ratio of the CNF. The CNFs were dispersed in deionized water and the heights of the sediments were measured after 1 week and used to assess the aspect ratio of the CNF_{19} , $\text{CNF}_{2.3}$, and $\text{CNF}_{4.4}$ suspensions. The aspect ratio was calculated as previously reported³⁸ from crowding number theory (Equation S1).

Foams Characterization

SEM images of the foam cross section were taken using a HITACHI TM-3000 (Germany) using a 5-kV electron beam at a magnification of $\times 500$.

High-resolution SEM images of the foams wall were taken using a JEOL JSM-7401F (United States) and a 0.5-kV electron beam at a magnification of $\times 5,000$ – $10,000$.

The apparent density, ρ , of the foams was calculated from the mass and the volume (height $\times \pi r^2$) of the foams, kept for 3 days at 50% RH and 295 K.

The porosity (Π) of the foams was determined from the skeletal (ρ_{skel})³⁰ and the apparent foam density (ρ_{app}).

Nitrogen sorption measurements were performed using ASAP 2020 (Micromeritics Instrument Corporation, Nocrass, GA, United States). The CNF foams were degassed at 80°C for 10 h.

XRD (Oxford Diffraction Xcalibur 3, Agilent Technologies, United States) was used to estimate the crystallinity index (Equation S3) and Hermans orientation parameter (Equation S4 and S5) of CNFs in the foam walls.

The foam orientation degree (Figure S6) was determined from at least three SEM images of each foam. ImageJ software and the plug-in OrientationJ were used to compare the orientation of each pixel with respect to neighboring pixels, and the frequency was plotted against the angle to give a histogram for each image. This was fitted to a Gaussian curve and the orientation index (f) was calculated from the full width at half-maximum (f_{whm}) of the curve.

DSC (Mettler Toledo 820, Sweden) was used to estimate the C_p (Figure S5) of three specimens for each foam at RH = 0 at temperatures ranging between -20°C and 50°C at 10 K min^{-1} .

Moisture Uptake

The water vapor sorption of the CNF foams under controlled RH and T was determined by measuring the weight change using a high-precision balance (BP 210 S, Sartorius, Germany) placed inside a humidity chamber as described previously.²⁶ Prior to the measurements, the foams were dried at 313 K and 20% RH. The moisture content (H_2O_w) as a function of RH (20%, 35%, 50%, 65%, and 80%) was assessed at 295 K. Each measurement lasted 6 h to ensure that steady state was reached, and the foam mass was measured every 5 min.

Thermal Conductivity Measurement

The thermal conductivities (λ , $\text{mW m}^{-1} \text{ K}^{-1}$) of the foams were measured using the TPS 2500 S Hot Disk Thermal Constants Analyzer in anisotropic mode. The transient plane sensor (6.4 mm in radius) was placed between two identical CNF foams (diameter, 4.1 ± 0.1 cm; height, 2.4 ± 0.2 cm) (Figure S4A). Good thermal contact between the sensor and the foams was ensured by putting a small weight onto the samples (Figure S4B).⁵⁰ The heating power was 20 mW and the measurement time was 10 s for each measurement. The foams were enclosed in a customized cell, allowing for the RH to be controlled (2%–80% RH).²⁶ Five independent measurements were performed at 15-min intervals for each RH at 295 K on three pairs of foam specimens. The thermal diffusivity and conductivity values (Equations 1 and S8–S12) of the anisotropic foams at different RH and T were measured using the wet C_p (Equation S12) and density of the foams as input.

GCMC and MD Simulations

The GCMC simulations were run in μVT ensemble, where μ (Equations S13 and S14) is the chemical potential, V is the volume, and T is the temperature of the system. The MD simulations were performed in $N\sigma T$ ensemble, where N is the number of particles inside the system and σ is the stress on the system.⁵¹

All simulations were performed with the LAMMPS MD package.⁵² The OPLS-AA⁵³ force field modified for carbohydrates was used for the fibrils with SPC/E⁵⁴ (extended Simple Point Charge) model for water. The parallel alignment of CNF was investigated by arranging four fibrils in a square pattern with periodic boundary conditions.

NEMD Simulations

The NEMD simulations were performed using the LAMMPS package.⁵² The consistent valence force field⁵⁵ potential was used to describe the bonding and non-bonding interactions within and between the cellulose molecules, and the SPC model⁵⁶ was used for water. For both Lennard-Jones potential and coulombic force, the cutoff distance was set as 14 Å and the time step was set as 0.5 fs. Fixed and periodic boundary conditions were adopted in the x and cross-plane (y and z; Figure 4A) directions, respectively. To impose a temperature gradient, two Langevin thermostats⁵⁷ with different temperatures (T_{high} and T_{low}) were applied to the two ends of the simulation system (Figure S11).

The simulation systems were first under isothermal-isobaric (NPT) ensemble for 50 ps, during which the entire system reached thermal equilibration and the stresses in all directions were fully relaxed. Then, the NEMD simulations were performed, the ΔT was calculated (Figure S11A), and the cumulative energy ΔE (Figure S11B) was used to calculate the heat flux.

SUPPLEMENTAL INFORMATION

Supplemental Information can be found online at <https://doi.org/10.1016/j.matt.2020.11.007>.

ACKNOWLEDGMENTS

We thank Kjell Jansson for helping us with HRSEM, Tamara L. Church for language proofreading and for valuable suggestions, and Korneliya Gordeyeva for relevant discussions.

L.B. acknowledges support from the Swedish Energy Agency (Energimyndigheten, project 2019-006749), Formas (project 2015-2032), and the Wallenberg Wood Science Center (WWSC). I.Z. acknowledges support of the Swedish Research Council (projects 2016-05990) and Åforsk. M.L. acknowledges support from the Swedish e-Research Centre (SeRC). The computations were performed on resources provided by the Swedish National Infrastructure for Computing (SNIC) at NSC and HPC2N.

AUTHOR CONTRIBUTIONS

V.A.K. and L.B. conceived and designed the study. V.A.K. and N.L. prepared the materials. V.A.K. characterized the CNF and the foams, performed the thermal conductivity measurements and analyzed the data, and wrote the first draft of the manuscript. P.M. performed the HRSEM characterization and contributed to the AFM imaging and XRD data analysis. J.S. conceived the NEMD study, S.H. performed the NEMD simulations, and J.S. and S.H. analyzed the data. I.Z. and M.L. conceived

the MD water intake simulations. M.G. performed the hybrid GCMC/MD simulations and I.Z., M.L., and M.G. analyzed the data. V.A.K. and L.B. wrote the manuscript with input from all co-authors.

DECLARATION OF INTERESTS

The authors declare no competing interests.

Received: June 26, 2020

Revised: September 22, 2020

Accepted: November 5, 2020

Published: November 27, 2020

REFERENCES

- Jelle, B.P. (2011). Traditional, state-of-the-art and future thermal building insulation materials and solutions - properties, requirements and possibilities. *Energy Build.* 43, 2549–2563.
- Fang, Z., Li, B., Liu, Y., Zhu, J., Li, G., Hou, G., Zhou, J., Qiu, X., et al. (2020). Critical role of degree of polymerization of cellulose in super-strong nanocellulose films. *Matter* 2, 1000–1014.
- Duong, H.M., and Nguyen, S.T. (2016). Chapter 15 nanocellulose aerogels as thermal insulation materials. In *Nano and Biotech Based Materials for Energy Building Efficiency* (SpringerNature), pp. 97–124.
- De France, K., Zeng, Z., Wu, T., and Nyström, G. (2020). Functional materials from nanocellulose: utilizing structure-property relationships in bottom-up fabrication. *Adv. Mater.* 2000657, 1–22.
- Usov, I., Nyström, G., Adamcik, J., Handschin, S., Schütz, C., Fall, A., Bergström, L., Mezzenga, R., et al. (2015). Understanding nanocellulose chirality and structure-properties relationship at the single fibril level. *Nat. Commun.* 6, 1–11.
- Martin-Martinez, F.J. (2018). Designing nanocellulose materials from the molecular scale. *Proc. Natl. Acad. Sci. U S A* 115, 7174–7175.
- Atalla, R.H., and Vanderhart, D.L. (1984). Native cellulose: a composite of two distinct crystalline forms. *Science* 223, 283–285.
- Molnár, G., Rodney, D., Martoia, F., Dumont, P.J.J., Nishiyama, Y., Mazeau, K., Orgéas, L., et al. (2018). Cellulose crystals plastify by localized shear. *Proc. Natl. Acad. Sci. U S A* 115, 7260–7265.
- Wada, M. (2002). Lateral thermal expansion of cellulose I β and III polymorphs. *J. Polym. Sci. B Polym. Phys.* 40, 1095–1102.
- Dri, F.L., Shang, S., Jr, L.G.H., Saxe, P., Liu, Z., Moon, R.J., Zavattieri, P.D., et al. (2014). Anisotropy and temperature dependence of structural, thermodynamic, and elastic properties of crystalline cellulose I β : a first-principles investigation. *Model. Simul. Mater. Sci. Eng.* 22, 1–28.
- Li, T., Song, J., Zhao, X., Yang, Z., Pastel, G., Xu, S., Jia, C., Dai, J., Chen, C., Gong, A., et al. (2018). Anisotropic, lightweight, strong, and super thermally insulating nanowood with naturally aligned nanocellulose. *Sci. Adv.* 4, 1–10.
- Balandin, A.A. (2011). Thermal properties of graphene and nanostructured carbon materials. *Nat. Mater.* 10, 569–581.
- Qiu, L., Wang, X., Su, G., Tang, D., Zheng, X., Zhu, J., Wang, Z., Norris, P.M., Bradford, P.D., Zhu, Y., et al. (2016). Remarkably enhanced thermal transport based on a flexible horizontally-aligned carbon nanotube array film. *Sci. Rep.* 6, 1–14.
- Jain, A., and McGaughey, A.J.H. (2015). Strongly anisotropic in-plane thermal transport in single-layer black phosphorene. *Sci. Rep.* 5, 8501.
- Robbins, A.B., Drakopoulos, S.X., Martin-Fabiani, I., Ronca, S., and Minnich, A.J. (2019). Ballistic thermal phonons traversing nanocrystalline domains in oriented polyethylene. *Proc. Natl. Acad. Sci. U S A* 116, 17163–17168.
- Song, N., Jiao, D., Ding, P., Cui, S., Tang, S., and Shi, L. (2016). Anisotropic thermally conductive flexible films based on nanofibrillated cellulose and aligned graphene nanosheets. *J. Mater. Chem. C* 4, 305–314.
- Luo, T., and Lloyd, J.R. (2012). Enhancement of thermal energy transport across graphene/graphite and polymer interfaces: a molecular dynamics study. *Adv. Funct. Mater.* 22, 2495–2502.
- Kobayashi, Y., Saito, T., and Isogai, A. (2014). Aerogels with 3D ordered nanofiber skeletons of liquid-crystalline nanocellulose derivatives as tough and transparent insulators. *Angew. Chem. Int. Ed.* 53, 10394–10397.
- Sakai, K., Kobayashi, Y., Saito, T., and Isogai, A. (2016). Partitioned air at microscale and nanoscale: thermal diffusivity in ultrahigh porosity solids of nanocellulose. *Sci. Rep.* 6, 20434.
- Chen, W., Li, Q., Wang, Y., Yi, X., Zeng, J., and Yu, H. (2014). Comparative study of aerogels obtained from differently prepared nanocellulose fibers. *ChemSusChem* 230026, 154–161.
- Jimenez-Saelices, C., Seantier, B., Cathala, B., and Grohens, Y. (2017). Spray freeze-dried nanofibrillated cellulose aerogels with thermal superinsulating properties. *Carbohydr. Polym.* 157, 105–113.
- Jiménez-Saelices, C., Seantier, B., Grohens, Y., and Capron, I. (2018). Thermal superinsulating materials made from nanofibrillated cellulose-stabilized Pickering emulsions. *ACS Appl. Mater. Interfaces* 10, 16193–16202.
- Chen, J., Huang, X., Zhu, Y., and Jiang, P. (2017). Cellulose nanofiber supported 3D interconnected BN nanosheets for epoxy nanocomposites with ultrahigh thermal management capability. *Adv. Funct. Mater.* 27, 1–9.
- Bendahou, D., Bendahou, A., Seantier, B., Grohens, Y., and Kaddami, H. (2015). Nanofibrillated cellulose-zeolites based new hybrid composites aerogels with super thermal insulating properties. *Ind. Crops Prod.* 65, 374–382.
- Guo, X., Wu, Y., and Xie, X. (2017). Water vapor sorption properties of cellulose nanocrystals and nanofibers using dynamic vapor sorption apparatus. *Sci. Rep.* 7, 1–12.
- Apostolopoulou-Kalkavrou, V., Gordeyeva, K., Lavoine, N., and Bergström, L. (2018). Thermal conductivity of hygroscopic foams based on cellulose nanofibrils and a nonionic polyoxamer. *Cellulose* 25, 1117–1126.
- Benítez, A.J., Torres-Rendon, J., Poutanen, M., and Walther, A. (2013). Humidity and multiscale structure govern mechanical properties and deformation modes in films of native cellulose nanofibrils. *Biomacromolecules* 14, 4497–4506.
- Kulasinski, K., Guyer, R., Derome, D., and Carmeliet, J. (2015). Water adsorption in wood microfibril-hemicellulose system: role of the crystalline-amorphous interface. *Biomacromolecules* 16, 2972–2978.
- Kulasinski, K. (2016). Effects of water adsorption in hydrophilic polymers. *Polym. Sci. Res. Adv. Pract. Appl. Educ. Asp.* 217–223.
- Wicklein, B., Kocjan, A., Salazar-Alvarez, G., Carosio, F., Camino, G., Antonietti, M., Bergström, L., et al. (2015). Thermally insulating and fire-retardant lightweight anisotropic foams based on nanocellulose and graphene oxide. *Nat. Nanotechnol.* 10, 277–283.
- Kriechbaum, K., Munier, P., Apostolopoulou-Kalkavrou, V., and Lavoine, N. (2018). Analysis

- of the porous architecture and properties of anisotropic nanocellulose foams: a novel approach to assess the quality of cellulose nanofibrils (CNFs). *ACS Sustain. Chem. Eng.* 6, 11959–11967.
32. Munier, P., Apostolopoulou-Kalkavoura, V., Persson, M., and Bergström, L. (2019). Strong silica-nanocellulose anisotropic composite foams combine low thermal conductivity and low moisture uptake. *Cellulose*, 1–12.
33. Lu, X., Arduini-Schuster, M.C., Kuhn, J., Nilsson, O., Fricke, J., and Pekala, R.W. (1992). Thermal conductivity of monolithic organic aerogels. *Science* 255, 971–972.
34. Budtova, T. (2019). Bio-based aerogels : a new generation of thermal superinsulating materials. In *Cellulose Science and Technology: Chemistry, Analysis, and Applications*, First Edition 2019, pp. 371–392.
35. Sadeghi, M.M., Jo, I., and Shi, L. (2013). Phonon-interface scattering in multilayer graphene on an amorphous support. *Proc. Natl. Acad. Sci. U S A* 110, 16321–16326.
36. Hung, S.W., Kikugawa, G., and Shiomi, J. (2016). Mechanism of temperature dependent thermal transport across the interface between self-assembled monolayer and water. *J. Phys. Chem. C* 120, 26678–26685.
37. Losego, M.D., Grady, M.E., Sottos, N.R., Cahill, D.G., and Braun, P.V. (2012). Effects of chemical bonding on heat transport across interfaces. *Nat. Mater.* 11, 502–506.
38. Varanasi, S., He, R., and Batchelor, W. (2013). Estimation of cellulose nanofibre aspect ratio from measurements of fibre suspension gel point. *Cellulose* 20, 1885–1896.
39. Munier, P., Gordeyeva, K., Bergström, L., and Fall, A.B. (2016). Directional freezing of nanocellulose dispersions aligns the rod-like particles and produces low-density and robust particle networks. *Biomacromolecules* 17, 1875–1881.
40. Deville, S. (2018). The lure of ice-templating Recent trends and opportunities for porous materials. *Scr. Mater.* 147, 119–124.
41. Anderson, A.M., and Worster, M.G. (2012). Periodic ice banding in freezing colloidal dispersions. *Langmuir* 28, 16512–16523.
42. Lagüela, S., Bison, P., Peron, F., and Romagnoni, P. (2015). Thermal conductivity measurements on wood materials with transient plane source technique. *Thermochim. Acta* 600, 45–51.
43. Zeng, S.Q., Hunt, A., and Greif, R. (1995). Transport properties of gas in silica aerogel. *J. Non. Cryst. Sol.* 186, 264–270.
44. Ruckdeschel, P., Philipp, A., and Retsch, M. (2017). Understanding thermal insulation in porous, particulate materials. *Adv. Funct. Mater.* 27, 1–11.
45. Collishaw, P.G., and Evans, J.R.G. (1994). An assessment of expressions for the apparent thermal-conductivity of cellular materials. *J. Mater. Sci.* 29, 2261–2273.
46. Hu, S., Zhang, Z., Jiang, P., Ren, W., Yu, C., Shiomi, J., Chen, J., et al. (2019). Disorder limits the coherent phonon transport in two-dimensional phononic crystal structures. *Nanoscale* 11, 11839–11846.
47. Saito, T., and Isogai, A. (2004). TEMPO-mediated oxidation of native cellulose. The effect of oxidation conditions on chemical and crystal structures of the water-insoluble fractions. *Biomacromolecules* 5, 1983–1989.
48. Saito, T., and Isogai, A. (2006). Introduction of aldehyde groups on surfaces of native cellulose fibers by TEMPO-mediated oxidation. *Colloids Surf. A Physicochem. Eng. Asp.* 289, 219–225.
49. Scandinavian pulp paper and board testing committee (2002). Total Acidic Group Content, 2002 (Scandinavian Pulp, Paper and Board Testing Committee), pp. 1–4.
50. Gustafsson, S.E. (1991). Transient plane source techniques for thermal conductivity and thermal diffusivity measurements of solid materials. *Rev. Sci. Instrum.* 62, 797–804.
51. Chen, M., Coasne, B., Guyer, R., Derome, D., and Carmeliet, J. (2018). Role of hydrogen bonding in hysteresis observed in sorption-induced swelling of soft nanoporous polymers. *Nat. Commun.* 9, 1–7.
52. Plimpton, S. (1995). Fast parallel algorithms for short-range molecular dynamics. *J. Comput. Phys.* Vol. 117, 1–19.
53. Kony, D., Damm, W., Stoll, S., and Van Gunsteren, W.F. (2002). An improved OPLS-AA force field for carbohydrates. *J. Comput. Chem.* 23, 1416–1429.
54. Soper, A.K. (1996). Empirical potential Monte Carlo simulation of fluid structure. *Chem. Phys.* 202, 295–306.
55. Dauber-Osguthorpe, P., Roberts, V.A., Osguthorpe, D.J., Wolff, J., Genest, M., and Hagler, A.T. (1988). Structure and energetics of ligand binding to proteins : *Escherichia coli* dihydrofolate reductase-trimethoprim , a drug-receptor system. *Proteins* 4, 31–47.
56. Berendsen, H.J.C., Postma, J.P.M., van Gunsteren, W.F., DiNola, A., and Haak, J.R. (1984). Molecular dynamics with coupling to an external bath. *Chem. Phys.* 81, 3684–3690.
57. Hu, S., Chen, J., Yang, N., and Li, B. (2017). Thermal transport in graphene with defect and doping : phonon modes analysis. *Carbon N. Y.* 116, 139–144.